

Molecular Ordering and Molecular Dynamics in Isotactic-Polypropylene Characterized by Solid State NMR

Toshikazu Miyoshi,* Al Mamun, and Wei Hu

Research Institute of Nanotechnology, National Institute for Advanced Industrial Science and Technology, Central 5-1 Higashi 1-1-1, Tsukuba, Ibaraki 305-8565, Japan

Received: September 7, 2009; Revised Manuscript Received: October 14, 2009

The order–disorder phenomenon of local packing structures, space heterogeneity, and molecular dynamics and average lamellar thickness, $\langle l \rangle$, of the α form of *isotactic* polypropylene (iPP) crystallized at various supercooling temperatures, ΔT , are investigated by solid-state (SS) NMR and SAXS, respectively. $\langle l \rangle$ increases with lowering ΔT , and extrapolations of $\langle l \rangle^{-1}$ versus averaged melting point, $\langle T_m \rangle$, gives an equilibrium melting temperature, $T_m^0 = 457 \pm 4$ K. High-power TPPM decoupling with a field strength of 110 kHz extremely improves ^{13}C high-resolution SS-NMR spectral resolution of the ordered crystalline signals at various ΔT . A high-resolution ^{13}C SS-NMR spectrum combined with a conventional spin–lattice relaxation time in the rotating frame ($T_{1\rho\text{H}}$) filter easily accesses an order–disorder phenomenon for upward and downward orientations of stems and their packing in the crystalline region. It is found that ordered packing fraction, f_{order} , increases with lowering ΔT and reaches a maximum value of 62% at $\Delta T = 34$ K. The ordering phenomenon of stem packing indicates that chain-folding direction changes from random in the disordered packing to order in the ordered packing along the $a \sin \theta$ axis under a hypothesis of adjacent re-entry structures. It is also found that f_{order} significantly increases prior to enhancement of lamellar thickness. Additionally, annealing experiments indicate that $\langle l \rangle$ is significantly enhanced after a simultaneous process of partial melting and recrystallization/reorganization into the ordered packing at annealing temperature ≥ 423 K. Furthermore, the center-bands only detection of exchange (CODEX) NMR method demonstrates that time–kinetic parameters of helical jump motions are highly influenced by ΔT . These dynamic constraints are interpreted in terms of increment of $\langle l \rangle$ and packing ordering. Through these new results related to molecular structures and dynamics, roles of polymer chain trajectory and molecular dynamics for the lamellar thickening process are discussed.

1. Introduction

Polymer crystallization changes random polymer chains into bilayer structures consisting of a folded polymer crystal and an amorphous region. Generally, lamellar thickness for semicrystalline polymers is proportional to the inverse of supercooling, $1/\Delta T$ ($\Delta T = T_m^0 - T_c$, where T_m^0 and T_c are equilibrium melting temperature and crystallization temperature, respectively), under solution and bulk crystallization.^{1,2} Many works focus on the lamellae thickening phenomenon and suggest that molecular dynamics contributes to the lamellar thickening process.^{3–8} Schmidt-Rohr and Spiess for the first time detected chain diffusion of polyethylene (PE) between crystal and amorphous regions by two-dimensional (2D) ^{13}C exchange NMR.⁹ Additionally, solid state (SS) NMR using magnetically anisotropic interactions has successfully revealed that PE,¹⁰ *isotactic*-polypropylene (iPP),¹¹ poly(oxymethylene) (POM),¹² poly(ethylene oxide) (PEO),¹³ and *isotactic*-poly(4-methyl 1-pentene) (iP4M1P),¹⁴ etc., commonly show helical jump motions in the crystalline region at mechanical α_c relaxation temperatures. This local dynamics includes rotational jumps and translations of stems and is an origin for chain diffusions between the crystalline and amorphous regions. Previous SS-NMR works^{9–14} gave a simple picture on the lamellar thickening process: Thermal activated stem dynamics results in thickening of

lamellae at high temperatures under both crystallization and annealing. Actually, the lamellar thickening process of PE depends on the morphology under annealing. Solution grown (SGC) and nascent crystals (NC) exhibit significant increases in lamellar thickness, $\langle l \rangle$, by annealing, while only melt grown crystals (MC) do not show a significant increase. Especially Rastogi et al. found a quantum jump of $\langle l \rangle$ in SC samples at annealing temperature above 383 K before melting points.^{4,5} Uehara et al.¹⁵ and Rastogi et al.^{16,17} investigated relationships between molecular dynamics and lamellar thickness in different morphologies under annealing. Uehara et al. deduced that entanglements of polymer chains interrupt lamellar thickening in MC.¹⁵ Rastogi et al. detected motional difference in the interfacial region between MC and SGC by residually anisotropic interactions.^{16,17} The latter authors suggested that interfacial rigidity facilitates chain diffusions which result in lamellar thickening in SGC. Additionally, former neutron scattering (NS) works indicated that the radius of gyration (R_g) in SGC is much smaller than that in melt and MG.¹⁸ These results indicate that there are clear differences in the amorphous structures and interfacial rigidity between the SGC and MC samples. There are many works in the NS intermediate range for investigating chain-level structural changes inside of PE crystals.¹⁹ However, interpretations on data are scattered. Hoffman et al. theoretically indicated that adjacent re-entry structures of PE in MC increase from 30 to 66% from regime III to I, respectively.¹

* Corresponding author. E-mail: t-miyoshi@aist.go.jp. Tel.: +81-298-61-9392. Fax: +81-298-61-4437.

Stereoregular polymers adopt helical structures with right (*R*) and left (*L*) hands in the crystalline region. Lateral groups of helical chains are not normal, but rather are tilted to the chain axis, irrespective of handedness. Therefore, upward (\uparrow) and downward (\downarrow) orientations exist independently of handedness. Stereoregular polymers can adopt one of four types of stem structures in the crystalline region, namely, R_u , R_d , L_d , and L_u , each of which shows identical rotational energy in isolated states. In several systems, order–disorder phenomena of the stem orientations and packing have been detected by X-ray diffraction (XRD)^{20–26} and SS-NMR.^{27–31} Most works focused on the α form of *i*PP and demonstrated that there is a statistical disorder in the stem orientations and packing at low T_c , and such a disorder decreases with an increase of T_c and almost disappears at very high T_c .^{23,25,26,30} The statistical disorder and complete order are called to be a full limit disorder and a full limit order, respectively. These stem orientations and packing results depending on supercooling are very important structures to investigate local structures of polymer chains inside of the crystal. We have further questions about these locally structural results in the α form of *i*PP: (i) Is it possible to form a complete ordering in the stem orientations and packing under bulk crystallization? (ii) What does ordering of the stem orientations and packing mean at chain-level structure? (iii) If stem orientations are intermediate between the two limiting structures, how are ordered and disordered structures distributed in the crystals? (iv) Is there a relationship between local structural ordering and lamellar thickness enhancement? (v) Is there a relationship between structures including lamellar thickness and packing order and dynamics? These questions were not addressed in the literature. The answers may be key factors for understanding of a mechanism of $1/\Delta T$ of lamellar thickness in the polymer crystals.

In this study, we investigate molecular level structure and molecular dynamics inside of the α form of *i*PP by SS-NMR. Initially, we re-evaluate the order–disorder phenomenon for the stem orientations and their packing in the α form of *i*PP with a high isotacticity sample under isothermal crystallization and annealing by conventional high-resolution ^{13}C SS-NMR incorporating an ^1H spin–lattice relaxation time in the rotating frame ($T_{1\rho\text{H}}$) filter. The relaxation filter eliminates the amorphous contribution to the spectrum. In this measurement, high power TPPM³² decoupling is applied for effective suppression of ^1H – ^{13}C dipolar interactions. The highly improved ^{13}C high-resolution SS-NMR spectrum properly evaluates intermediate structures between the two limiting structures and ordered packing fraction, f_{order} , under both isothermal crystallization and annealing. Consequently, it is found that a significant amount of disorders in the stem orientations is included even at high T_c and T_a . Moreover, we discuss chain-level structure changes based on the stem orientations and chain-folding rules.³³ This will demonstrate that ordering of polymer chain arrangement occurs with increasing T_c . Second, we explore space heterogeneity between the ordered and disordered packing areas by ^1H $T_{1\rho\text{H}}$. The obtained results indicate that ordered and disordered packing areas form domain structures on a scale ~ 9 nm. Third, we characterize lamellar thickness, $\langle l \rangle$, of the α form by SAXS and treat supercooling and annealing effects on $\langle l \rangle$ and f_{order} . As a result, it is found from a unique relationship between f_{order} and $\langle l \rangle$ that molecular ordering occurs prior to lamellar thickness enhancement under crystallization and annealing. Fourth, we investigate correlation time $\langle \tau_c \rangle$ and activation energy of helical jump motions of stems in the α form of *i*PP by applying center-bands only detection of exchange (CODEX)

TABLE 1: Averaged Lamellar Thickness, $\langle l \rangle$, Averaged Melting Point, $\langle T_m \rangle$, and Ordered Packing Fraction, f_{order} , for the α Form of *i*PP Crystallized at Various ΔT

sample name	$\Delta T/\text{K}$	$\langle l \rangle/\text{nm}$	$\langle T_m \rangle/\text{K}$	$f_{\text{order}}/\%$
<i>i</i> PP_ΔT84	84	9.3	427.5	0
<i>i</i> PP_ΔT74	74	9.7	429.2	13
<i>i</i> PP_ΔT64	64	10.0	429.4	21
<i>i</i> PP_ΔT54	54	10.8	431.1	38
<i>i</i> PP_ΔT44	44	12.6	437.5	50
<i>i</i> PP_ΔT39	39	15.6	441.5	56
<i>i</i> PP_ΔT34	34	19.4	446.2	62
<i>i</i> PP_ΔT29	29	20.9	446.3	59
<i>i</i> PP_ΔT27	27	23.9	448.2	58
<i>i</i> PP_ΔT24	24	22.7	447.2	59

NMR.³⁴ As a result, it is found that there are large variations in $\langle \tau_c \rangle$ and activation energy of stem dynamics depending on supercooling. Through these experimental evidences, we will conclude that not only stem dynamics but also molecular level ordering inside of the crystal play important roles for lamellar thickness enhancement at very high temperatures.

2. Experimental Section

2.1. Sample. Unfractionated *i*PP with an average molecular weight of $M_w = 360\,000$ and a polydispersity of $M_w/M_n = 3.3$ and isotacticity, $\langle mmmmm \rangle = 97\%$, was purchased from Polysciences, Inc. We did not further purify the sample. The sample was melted between two cover glasses on a hot stage. The thickness of the sample was controlled for 0.2 mm by inserting a metal spacer between the cover glasses. The sample was first melted and then crystallized several times to erase the previous thermal history. In a typical experiment, the sample was melted for 5 min at 493 K. After that, the samples were rapidly transferred to another hot stage that was preset to the required crystallization temperature, T_c 's of 373, 383, 393, 403, 408, 413, 418, 423, 428, 430, and 433 K, to allow an isothermal crystallization for 2, 2, 2, 4, 4, 24, 24, 288, 288, 288, and 408 h, respectively, under nitrogen atmosphere. The sample was completely solidified, and full crystallization was confirmed by polarized optical microscope (POM). T_m^0 was determined to be 457 ± 4 K in terms of a Gibbs–Thomson equation using $\langle l \rangle$ and melting temperatures obtained by DSC. *i*PP samples crystallized at $T_c < 413$ K show melt and recrystallization during a heating in DSC experiments. Then, we used only $\langle l \rangle$ and T_m data above $T_c = 413$ K. The samples crystallized at different ΔT are labeled by ΔT ; e.g., the *i*PP sample crystallized at $\Delta T = 34$ K is labeled as “*i*PP_ΔT34” (Table 1). An absence of other polymorphs, β , and γ phases in all samples was confirmed by XRD. Additionally, we made the melt-quenched sample into icy water and subsequently annealed the samples at 373 K for 2 h. This is the standard sample for the annealing experiments. Furthermore, we annealed the samples at target temperature of 373–433, 438, and 443 K for 24, 72, and 144 h, respectively.

2.2. SS-NMR. 2.2.1. ^{13}C CPMAS and $T_{1\rho\text{H}}$ Measurements. The ^{13}C SS-NMR experiments were carried out on a BRUKER AVANCE300 spectrometer, equipped with a 4 mm VT CPMAS NMR probe. The ^1H and ^{13}C carrier frequencies are 300.1 and 75.6 MHz, respectively. The MAS frequency was set to 4000 ± 3 Hz. The 90° pulses for ^1H and ^{13}C were 4.5–5.0 μs . The recycle delay and cross-polarization (CP) time were 2 s and 1 ms, respectively. High-power ^1H TPPM decoupling with a field strength of 110 kHz was used during an acquisition time of 160 ms. Such severe conditions in decoupling allow us to properly detect ordered signals in the crystalline region. The chemical shift was referenced to the CH signal of adamantane

(29.5 ppm) as an external reference. ^{13}C spin–lattice relaxation time in the laboratory frame ($T_{1\text{C}}$)²⁹ and $T_{1\rho\text{H}}$ measurements^{30,35} has been used for selective observation of pure crystalline signals for *i*PP at ambient temperatures. In this study, we utilized a $T_{1\rho\text{H}}$ filter under a spin-locking (SL) field strength of 55 kHz for a selective observation of the pure crystalline signals. All the experiments were carried out at an ambient temperature.

2.2.2. CODEX. The CODEX experiments utilize the recoupling of the chemical shift anisotropy (CSA) interaction by 180° pulse trains in the two evolution periods sandwiching a mixing period, t_{mix} .³⁴ The effect is a signal decay due to the dephasing of magnetization brought about by changes in orientation-dependent CSA due to a reorientational dynamic process during t_{mix} . The magnetization evolves during the initial evolution period $Nt_r/2$ (where $N = 2, 4, 6, \dots$) under the orientation-dependent CSA interaction, which is recoupled by two successive 180° pulses per MAS rotation period, t_r . The magnetization after the first evolution period is stored along the z direction by a 90° pulse and does not dephase during t_{mix} (which must be set to an integer multiple of t_r). The magnetization evolves again after the 90° readout pulse during the second evolution period ($Nt_r/2$) and is refocused at its end. The second mixing period t_z serves as a z -filter and permits the cancellation of longitudinal relaxation. In our experiments, t_z was set to one t_r . After applying the last 90° pulse, the signal is detected under ^1H TPPM decoupling. If there is no molecular motion during t_{mix} , the evolutions in the two evolution periods will cancel each other, and there will be no decay of the signal intensity. If there is molecular motion during t_{mix} , the orientation-dependent frequency before and after t_{mix} will be different, and the magnetization will not completely be refocused. The resulting dephasing leads to a decay of the signal intensity in the exchange spectrum (S). To remove the T_1 and spin–spin relaxation (T_2) effects during t_{mix} and Nt_r , a reference spectrum is acquired. It is obtained simply by interchanging t_{mix} and t_z . The signal intensity in the reference spectrum (S_0) is not sensitive to exchange processes but is only dominated by T_1 , T_2 , and pulse length errors. The motional correlation time and information about the motional geometry can be obtained by plotting the ratio (S/S_0) versus t_{mix} and (S/S_0) versus Nt_r , respectively. A more detailed description of the CODEX experiment can be found in ref 34. The MAS frequency was 4000 ± 3 Hz. The ^1H rf field strength for CW decoupling during the ^{13}C 180° pulse with a pulse length of $15\ \mu\text{s}$ was set to 100 kHz. The evolution time for CSA was set to 2 ms. All other rf parameters were the same as for the CPMAS experiments. The reference and exchange experiments were obtained alternatively by every 128 transients, to suppress drift of the NMR spectrometer. Totally, each spectrum was obtained by accumulating 1536 transients. The total experimental time for mixing-time dependence up to 4 s was approximately 32 h. The total experimental time of a typical Nt_r experiment was about 18 h. The temperature in the sample was carefully calibrated by the temperature dependence of the ^{207}Pb chemical shift of $\text{Pb}(\text{NO}_3)_2$.³⁶

2.3. SAXS. SAXS studies were carried out using Cu K α radiation generated by a Rigaku Ultrax 4153A 172B X-ray diffractometer and a point-focusing SAXS camera. The camera length used was 740 mm, and the images were recorded using an image plate (IP) with an exposure time of 2.5 h. Digitized data were then read from the IP using the image plate reader. Using IP, a very small change in SAXS patterns could be obtained with a very short exposure time. The corrected pattern of an empty sample holder was subtracted from each pattern.

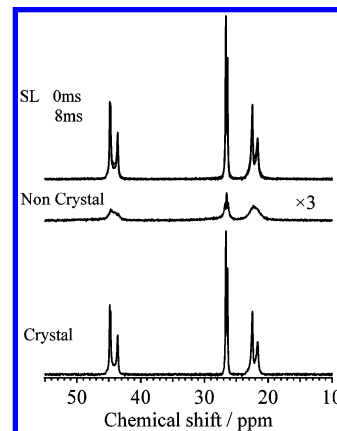


Figure 1. ^{13}C CPMAS NMR spectra for the α form of *i*PP crystallized at $\Delta T = 34$ K. Noncrystalline (middle) and pure crystalline components (bottom) are obtained by linear combinations of two spectra obtained under spin-locking (SL) times of 0 and 8 ms (top). Noncrystalline signals are vertically amplified by 3-fold.

To calculate the long period and lamellar thickness, a correlation-function method by Rigaku R-axis software was used.

2.4. DSC. All the samples were measured with an updated computer interfaced Perkin-Elmer DSC-7. Both temperature and heat-flow levels were corrected by standard materials. Measurements of the melting points were performed at a heating rate of 10 K/min. To prevent thermal degradation, nitrogen gas was circulated around the sample pan. The calorimeter was calibrated following the standard procedures established in our laboratory. The melting temperatures are shown in Table 1 and are used for determination of T_m^0 .

3. Results

3.1. Ordered and Disordered Packing by ^{13}C High-Resolution SS-NMR. In semicrystalline polymers like *i*PP, the crystalline signals dominate the ^{13}C CPMAS NMR spectrum (SL = 0 ms), and a typical example is shown in the top of Figure 1. $T_{1\rho\text{H}}$ of *i*PP used in this study roughly shows two components of 3–5 and 34–110 ms, depending on ΔT . The former and latter are attributed to relaxations of the noncrystalline and crystalline components.³⁵ The top of Figure 1 shows ^{13}C CPMAS NMR spectra for *i*PP ΔT_{34} with and without the spin-locking filter of 8 ms. Noncrystalline components are suppressed by a $T_{1\rho\text{H}}$ filter. Linear combinations of two spectra produce pure noncrystalline and pure crystalline signals. At $\Delta T = 34$ K, we amplified filtered signals by 1.08-fold, and noncrystalline signals were obtained by subtracting the filtered spectrum from the nonfiltered one as illustrated in the middle of Figure 1. Similarly, pure crystalline signals are obtained by subtraction of the noncrystalline signals amplified by 0.35-fold from the filtered crystalline-rich spectrum. The bottom of Figure 1 shows pure crystalline signals obtained by linear combinations. In this work, all ^{13}C CPMAS pure crystalline signals are obtained in terms of linear combinations. The amplified factor depends on $T_{1\rho\text{H}}$ values in the systems.

Figures 2(a) and (b) show two limiting packing structures of the α form determined by XRD,²¹ and 2(c) shows ^{13}C CPMAS NMR spectra for the α form in MC samples at various ΔT . The spectral heights for the crystallized samples were vertically amplified for giving the same heights with a peak height of the CH_2 signal for the annealed sample at 44.2 ppm. The annealed sample at $T_a = 373$ K shows structureless and broad signals, corresponding to a full limit disorder.^{21,28} The observed broad signals are attributed to inhomogeneous line broadening due to

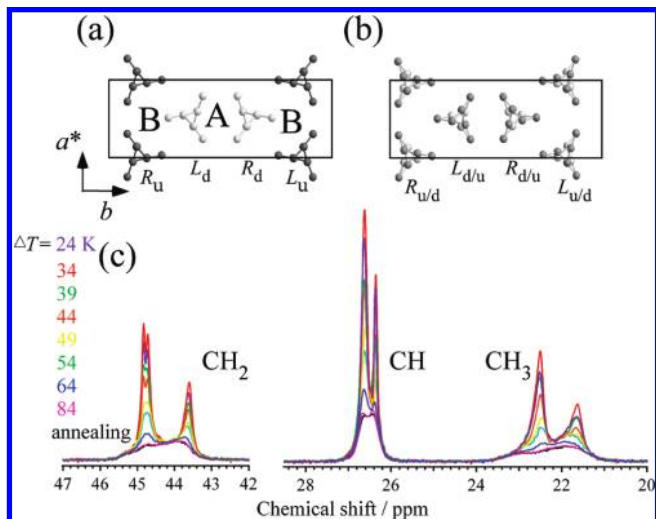


Figure 2. Unit-cell structures in (a) a full limit order and (b) a full limit disorder for the α form of *iPP*.²¹ Two types of packing structures denoted as A and B in a full limit order. (c) The ^{13}C CPMAS NMR spectra for the pure α form of *iPP* depending on ΔT and annealed at 373 K after melt quenching.

variations of local upward and downward orientations. At $\Delta T = 64$ K, newly narrowed doublet signals appear on the disordered line shapes, and the doublet signals grow in all functional signals with lowering ΔT . All the functional signals show maximum intensities for the doublet at $\Delta T = 34$ K. The observed doublet line shapes are direct NMR evidence for local ordering of the packing structures.^{28–31} The observed tendency is consistent with the former SS-NMR results.^{29–31} However, there is a large difference between current and former SS-NMR results. Ordered packing signals in this work are much narrower and much stronger intensities than those in the former SS-NMR ones. Strong TPPM decoupling with a field strength of 110 kHz and a long acquisition of ~ 160 ms highly improves spectral resolutions of the ordered signals. Thus, it is easy to indicate that our samples include much higher content of ordered packing than the former SS-NMR results,^{29–31} and at the same time a significant amount of the disordered components also exist even at very high T_c . As a result, highly improved ^{13}C resolutions reject former SS-NMR conclusions^{29–31} in which stem orientations and their packing are close to a nearly full limit order at very high T_c .

Pure ordered structures are simply obtained by subtraction of the structureless line shape corresponding to a full limit disorder from the observed spectra at various ΔT . For all the signals, the subtracted line shapes show doublet signals with an intensity ratio of 2:1 (data are not shown). This intensity ratio is consistent with the ideal ratio for “a full limit order” expected by Bunn et al.²⁸ The 2:1 intensity ratios correspond to two types of chain packing labeled by A and B sites in Figure 2(a). Quantitative analysis of order–disorder fractions will be shown after correction of relaxation effects during a spin-locking filter.

In addition, superior SS-NMR resolution provides a further local structure for the ordered packing structure. The downfield CH_2 signal shows a further splitting into the doublet below $\Delta T = 44$ K. This means that two CH_2 carbons in A sites in Figure 2(a) are magnetically inequivalent in a full limit order, and smaller supercooling allows stems to have better packing even in ordered packing structures during crystallization. This splitting was previously expected in quantum chemical calculations based on a full limit order by Aoki et al.³¹

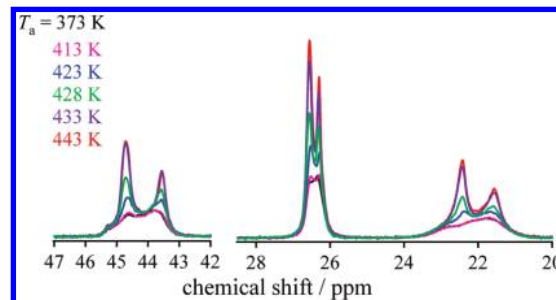


Figure 3. ^{13}C CPMAS NMR spectrum for the α form of *iPP* annealed at different T_a .

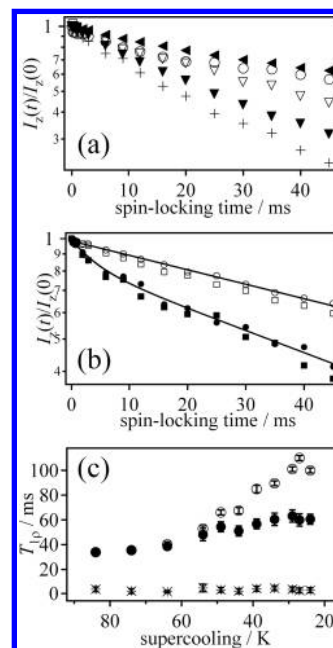


Figure 4. (a) $T_{1\rho\text{H}}$ decaying curves for the α form of *iPP* crystallized at $\Delta T = 84$ (+), 64 (▼), 50 (▽), 34 (○), 29 K (solid triangle pointing left). The curves obtained by peak-top intensity for the ^{13}C CH_2 signal at the downfield side of double ones. (b) $T_{1\rho\text{H}}$ relaxation curves for *iPP* $_{\Delta T29}$, obtained by peak height (■ and □) and peak area analyses (● and ○). Open and filled symbols showing the relaxations for the ordered and the disordered-rich packing areas, respectively. (c) ΔT dependence of three $T_{1\rho\text{H}}$ component values for ordered (○), disordered packing areas, (●) and noncrystalline components (×) obtained through the ^{13}C CH_2 signal by peak area analysis and the least-squares fitting. The fitting errors showing error bars.

Figure 3 shows annealing effects on ^{13}C CPMAS NMR spectra for the α form at different annealing temperature, T_a . Up to 413 K, there is no line-shape change in all functional signals, keeping disordered packing and orientations. Above 423 K, ordered packing grows in a limited temperature range of 423–433 K. It should be noted that ordered signals obtained by annealing give much broader ^{13}C line widths than those by isothermal crystallization. This suggests that ordered structures after rearrangement of the stem orientations by annealing are relatively disordered in comparison to the stem packing by isothermal crystallization.

3.2. $T_{1\rho\text{H}}$ Values and Space Heterogeneity. Supercooling effects on the $T_{1\rho\text{H}}$ relaxation behaviors are shown in Figure 4(a). The $T_{1\rho\text{H}}$ relaxations are obtained through peak height of the CH_2 doublet signals at the downfield side. The relaxations of crystalline regions become slower with lowering ΔT . Figure 4(b) shows the $T_{1\rho\text{H}}$ relaxation behaviors for *iPP* $_{\Delta T29}$, which are obtained through peak heights of the ^{13}C downfield signals of doublet ones (□) and ^{13}C minimum intensity at doublet valley

(■). The relaxation behaviors highly depend on the positions. The former is approximately described in terms of single exponential decay. This is dominated by relaxation in the ordered packing. On the other hand, the latter shows double exponential behavior. They are attributed to the disordered packing and the noncrystalline components. To evaluate the relaxation of different packing structures, peak deconvolution was also performed. Here, a series of relaxation data for the ordered packing were produced by subtraction of arbitrarily amplified relaxation data sets for a full limit disorder at $\Delta T = 84$ K from a series of relaxation spectra at various ΔT . Figure 4(b) shows one example for the relaxation behaviors for *iPP* ΔT_{29} analyzed by peak deconvolution. The open and filled circle symbols show pure ordered and disorder-rich relaxations, respectively. The results are almost the same as the results obtained by peak height. At high ΔT , however, the ordered packing fraction decreases, and simple peak-height analysis for ordered packing relaxations is dominated by relaxations of disordered structures. On the other hand, peak deconvolution analysis does not suffer from such a problem. Thus, all relaxation data were analyzed in terms of peak deconvolution. The obtained results are shown in Figure 4(c). The noncrystalline components show $T_{1\rho H} = 3\text{--}5$ ms with errors within 2 ms, irrespective of ΔT . $T_{1\rho H}$ values in disordered packing increase from 34 ± 2 to 64 ± 7 ms with lowering ΔT . $T_{1\rho H}$ values for ordered packing significantly increase from 40 ± 2 to 110 ± 4 ms. Through the obtained results, we obtain two findings in temperature dependence of the $T_{1\rho H}$ values. One is inconsistency between $T_{1\rho H}$ values in two types of packing structures at low $\Delta T \leq 54$ K. Another is significant enhancement in $T_{1\rho H}$ values in the ordered packing structures at low ΔT . Similar results were obtained in annealed samples. At $T_a = 443$ K, ordered and disordered areas show $T_{1\rho H} = 95 \pm 4$ and 54 ± 3 ms, respectively.

The observed variations of $T_{1\rho H}$ values for the ordered packing and the disordered one are explained in terms of intrinsic $T_{1\rho H}$ values, crystal size (lamellar thickness), and spatial connectivity among noncrystalline, ordered packing, and disordered packing areas. The observed inconsistency between $T_{1\rho H}$ values in the ordered and disordered packing at low ΔT is simply related to spatial heterogeneity between the two structures. For instance, the disordered region in *iPP* ΔT_{29} shows that a $T_{1\rho H}$ value of 64 ms is much shorter than that for ordered packing (110 ms). Namely, $T_{1\rho H}$ for the disordered region is much shorter than effective spin-diffusion time, T_{SD} , between the two structures. The spin-diffusion time between two systems provides average length scales $\langle r \rangle$ between the two structures by a relation, $\langle r \rangle = (4DT_{SD})^{1/2}$, in the two-dimensional case,³⁷ where D is the diffusion constant between the two structures. VanderHart et al. reported $D = 0.7$ nm²/ms for the α form of *iPP*.³⁵ This value is comparable to a reported diffusion constant, $D = 0.8$ nm²/ms, for other rigid systems.³⁸ Under spin-locking condition, D is reduced to half of a normal D value. Here we use $D = 0.35$ nm²/ms. T_{SD} is not obtained in simple $T_{1\rho H}$ measurements. However, we know a lower limit of T_{SD} using a following relation of $T_{SD} \geq \text{short } T_{1\rho H}$ in the heterogeneous system. $T_{1\rho H}$ is inserted into the above spin-diffusion equation instead of T_{SD} . Therefore, a lower limit of heterogeneity size of ~ 9 nm is obtained for *iPP* ΔT_{29} . At high ΔT , the $T_{1\rho H}$ value for the disordered packing is consistent with that for ordered packing. Consistent values between two packing structures cannot allow us to verify whether two structures show an intimate mixing on stem levels or not. This is a limitation of the $T_{1\rho H}$ measurement on spatial analysis. Actually, noncrystalline

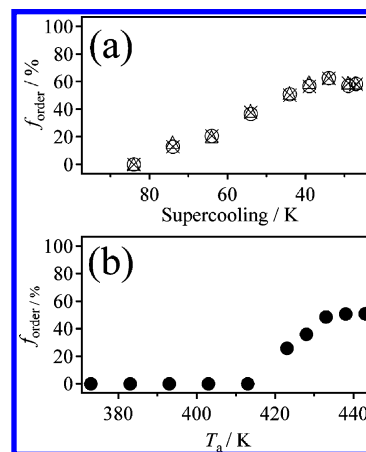


Figure 5. ΔT dependence of f_{order} obtained (a) through CH_2 (○), CH_3 (△), and averaged values through three functional signals (×) under isothermal crystallization and (b) through all the signals (●) under annealing.

components influence the $T_{1\rho H}$ results of the crystalline regions by spin diffusion. The noncrystalline components always show much smaller $T_{1\rho H}$ values than those in the crystalline regions. Therefore, smaller $T_{1\rho H}$ for the noncrystalline components is a sink source for the crystalline relaxations. Lowering ΔT leads to significant enhancement in $T_{1\rho H}$ values for the ordered packing structure. This phenomenon is interpreted in terms of isolation of the crystal lamellae from the amorphous region, namely, lamellar thickening. The relaxation differences between ordered and disordered areas indicate that lamellar thickness of ordered packing is effectively enhanced compared with that for disordered packing at very high T_c . This implication indicates that two different structures (packing structure and lamellar thickness) in different dimensions and length scales are highly correlated with each other. Additionally, under annealing, ordered and disordered areas also show domain structures $> \sim 9$ nm. This result indicates that replacements of wrong stem orientations occur via melt–recrystallization. The melt and recrystallization process was previously suggested by DSC.²⁴

3.3. Precise Analysis on Ordered Packing Fraction, f_{order} . Here, we evaluate f_{order} based on the SS-NMR results. In this work, we used the CP technique combined with a $T_{1\rho H}$ relaxation filter for obtaining pure crystalline signals through three functional signals. ^{13}C signal intensity is modulated by cross-relaxation time, T_{CH} , and two relaxation factors, $T_{1\rho H}$, and ^{13}C spin–lattice relaxation time in the rotating frame, $T_{1\rho C}$. Under the conditions of $T_{\text{CH}} \ll T_{1\rho C}$, the $T_{1\rho C}$ effect can be ignored. The build-up curve is approximately analyzed in terms of $I(t)/I(\text{eq}) = (\exp(-t/T_{\text{CH}}) - \exp(-t/T_{1\rho H}))(1 - T_{\text{CH}}/T_{1\rho H})^{-1}$. At $\Delta T = 84$ K, CH and CH_2 and CH_3 signals showing $T_{\text{CH}} = 0.1$ and 0.2 ms, respectively, are well consistent with T_{CH} values for CH and CH_2 signals (0.1 ms) and the CH_3 signal (0.2 ms) at $\Delta T = 84$ K. Thus, CP does not distort ordered and disordered packing fractions in the rigid systems. Only correction due to relaxations during a spin locking is necessary to get an accurate f_{order} . As shown above, both $T_{1\rho H}$ values in the two regions are much longer than the relaxation-filter time of 8 ms. For example, $T_{1\rho H}$ values are 60 and 110 ms for the disordered and ordered packing areas, respectively, for *iPP* ΔT_{29} . This condition gives a maximum correction factor of 1.5% in this work. The properly corrected f_{order} values are evaluated through CH_2 (○), CH_3 (△), and all three signals (×) and are plotted as a function of ΔT in Figure 5(a) and are also listed in Table 1. This plot demonstrates that individual function signals show similar f_{order} values in the investigated temperature ranges and reach a maximum value

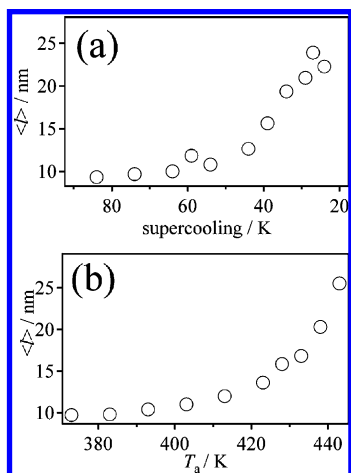


Figure 6. $\langle l \rangle$ versus (a) supercooling under isothermal crystallization and (b) T_a under annealing.

of 62% within experimental errors of 2% at $\Delta T = 34$ K. Additionally, increasing behaviors of f_{order} in annealing experiments are highly different from that under crystallization. f_{order} suddenly increases in the temperature range of 423–433 K, and f_{order} is saturated at $\sim 51\%$ above 433 K (Figure 5(b)).

There are two important findings in absolute value of f_{order} and temperature dependence of f_{order} at high-temperature regions compared with former XRD results.^{23,25,26} Our experiments show maximum values of $f_{\text{order}} = 62$ and 51% under crystallization and annealing, respectively. These values are much smaller than those by former XRD analyses ($f_{\text{order}} = \sim 100\%$ ^{23,26} and $90\text{--}95\%$ ²⁵). The observed differences between the current work and former work are very large. One may say that the difference is attributed to samples and their preparations. We do not agree with this opinion. Rather, it is naturally concluded that the polymer crystallization process includes more or less structural disorders, and it is impossible to reach a full limit order under isothermal crystallization. Later, I will consider these structural points in more detail. Here, we concentrate on the XRD and current SS-NMR methods. For XRD analysis, XRD requires a long-range order. Thus, XRD does not detect structures without long-range order. Auriemma et al. pointed out this point.²⁵ Additionally, XRD observes only very minor reflection changes of hkl with $h + k = \text{odd}$. These minor reflections are effected by the amorphous halo and backgrounds. These are disadvantages for XRD analysis on heterogeneous systems. On the other hand, SS-NMR does not require periodicity. Additionally, highly improved resolutions sensitively detects order–disorder line shapes. Additionally, the incorporated relaxation filter effectively eliminates the amorphous contributions. These differences between two different methods may result in a large difference in f_{order} values.

Another point is f_{order} at very high T_c . Under isothermal crystallization, Radhakrishnan et al. reported that f_{order} reaches a maximum value at $T_c = 423$ K, and f_{order} significantly drops at further high temperatures.²³ Nakamura et al. reported that f_{order} keeps a maximum even at further high T_c .²⁶ Our experimental evidence also indicates “saturation” of f_{order} at very high temperatures under crystallization and annealing. The observed drop in the former work²³ should be attributed to an insufficient crystallization time. Stem orientations and their packing are minimum scale structures of the polymer crystals at various length scales. Our experimental results indicate significant amounts of the disorders exist even at very high T_c and T_a .

3.4. $\langle l \rangle$ versus f_{order} . Figures 6(a) and (b) show $\langle l \rangle$ of the α form of *i*PP under isothermal crystallization and annealing,

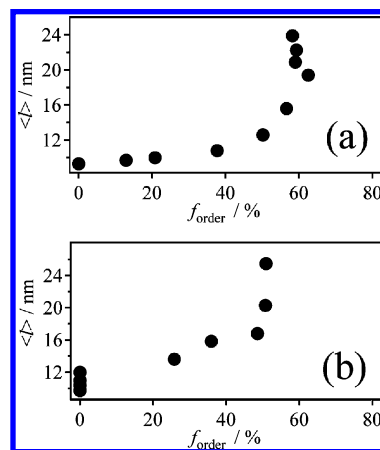


Figure 7. $\langle l \rangle$ versus f_{order} under (a) isothermal crystallization and (b) annealing.

respectively, obtained by SAXS. Both experimental results show that there are significant enhancements in $\langle l \rangle$ at very high T_c and T_a . In the annealing experiments, lamellar thickening occurs at temperatures above 423 K. Thus, lamellar thickening occurs after melt and recrystallization.

Figure 7(a) shows $\langle l \rangle$ as a function of f_{order} under isothermal crystallization. It is found that there is a unique relationship between them. An initial increase of $f_{\text{order}} \leq 50\%$ does not almost enhance $\langle l \rangle$ (only slightly enhanced by ~ 3 nm). However, $\langle l \rangle$ significantly increases in the limited region of $50 \leq f_{\text{order}} \leq 60\%$. This means that local ordering of packing takes place prior to thickening of the crystal lamellae under isothermal crystallization. The observed relationship between $\langle l \rangle$ and f_{order} suggests that a further small ΔT results in much thicker lamellar in ordered packing areas. In fact, Maiti et al.³⁹ and Yamada et al.^{40,41} observed extremely thicker crystal lamellae with a thickness of ~ 60 nm at very low ΔT for an extremely long crystallization time of several months.

Additionally, comparison of $\langle l \rangle$ and f_{order} under annealing gives a clearer view on importance of structural ordering. In annealing experiments, we prepared a full limit disorder by melt quenching into icy water and subsequent annealing at 373 K. If there is no relationship between stem orientations and $\langle l \rangle$, $\langle l \rangle$ increases without enhancement of f_{order} . Actually, below 423 K, f_{order} is invariant and $\langle l \rangle$ increases by only ~ 3 nm (Figure 7(b)). This is a pure annealing effect and very minor enhancement. Above 423 K, f_{order} initially increases in the limited range of 423–433 K. Enhancement in $\langle l \rangle$ follows the f_{order} increment at temperatures above 423 K. This curvature is quite similar to that in crystallization (Figure 7(a)). Thus, annealing experiments indicate that rearrangement of local structures inside of the crystals highly contributes to enhancement of $\langle l \rangle$. Therefore, two different structures with different length scales and dimensions are not independent of each other. This view is supported by the $T_{1\rho H}$ results, indicating that ordered packing areas have thicker lamellae than that for disordered packing areas.

3.5. Molecular Dynamics of Crystallization Stems Depending on Supercooling. The lamellar thickening process is highly related to molecular dynamics in the crystalline region. Previous ^2H NMR showed that the α form of *i*PP exhibits helical jump motions with a jump angle of 120° .¹¹ Here, we investigate supercooling effects on stem dynamics of the α form of *i*PP. Figure 8 shows N_{tr} dependence of the CODEX intensity ratio, (S/S_0) , for the ordered packing region of *i*PP- ΔT_{34} under t_{mix} of 200 ms at 411 K and simulation results with different jump angles of ψ . For simulation, we use the principal values and

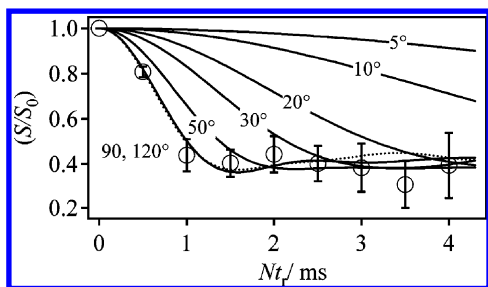


Figure 8. (a) CODEX Nt_r dependence for (S/S_0) intensity ratios for the ^{13}C CH_2 (O) for a fixed $t_{\text{mix}} = 200$ ms at 411 K and simulation assuming helical jump motions with different jump angles, ψ (solid (jump angles, $\psi = 5, 10, 20, 30, 50$, and 120°) and dotted ($\psi = 90^\circ$) curves).

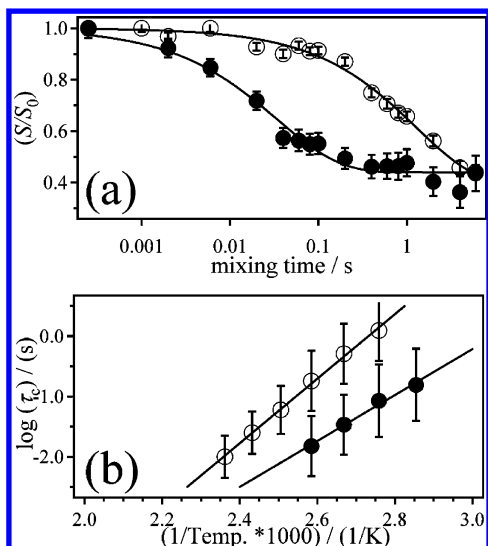


Figure 9. (a) CODEX t_{mix} dependence for (S/S_0) ratios for the ^{13}C CH_2 signal for $i\text{PP}_{\Delta T34}$ (O) and $i\text{PP}_{\Delta T84}$ (●) at 368 K. The solid lines showing best fitting ones to the experimental data, using $1 - a(1 - \exp(-(t_{\text{mix}}/\langle\tau_c\rangle)^\beta))$. (b) Arrhenius plot of $\langle\tau_c\rangle$ for $i\text{PP}_{\Delta T34}$ (O) and for $\Delta T84$ (●) with best fitted values of 102 ± 5 and 72 ± 4 kJ/mol, respectively.

axis orientations of CSA of ^{13}C CH_2 determined by Nakai et al.⁴² Our experimental data (O) are well reproduced by simulations with $\psi = 90^\circ$ (dotted curve) and 120° (solid curve). This dynamic geometry is well consistent with a jump angle of 120° due to helical jumps of 3_1 helices of $i\text{PP}$.

Previous ^2H NMR, however, could not investigate temperature dependence of stem dynamics due to very short ^2H T_1 .¹¹ Figure 9(a) shows CODEX t_{mix} dependence of (S/S_0) signal intensities for $i\text{PP}_{\Delta T84}$ (●) and the ordered packing for $i\text{PP}_{\Delta T34}$ (O) at 368 K. The CODEX decaying curves were analyzed using a following equation of $(S/S_0(t_{\text{mix}})) = 1 - a(1 - \exp(-(t_{\text{mix}}/\langle\tau_c\rangle)^\beta))$,³⁴ where a is related to the available site number of dynamics, p , $a = (p - 1)/p$; $\langle\tau_c\rangle$ is correlation time of molecular dynamics; and β is the stretched distribution parameter, $0 < \beta \leq 1$. The best fitting results to the experimental data give $a = 0.58 \pm 0.02$, $\langle\tau_c\rangle = 34.1 \pm 0.5$ ms, and $\beta = 0.62 \pm 0.07$ for $i\text{PP}_{\Delta T84}$ and $a = 0.61 \pm 0.04$, $\langle\tau_c\rangle = 1270 \pm 20$ ms, and $\beta = 0.64 \pm 0.03$ for the ordered packing for $i\text{PP}_{\Delta T34}$, respectively. The obtained a values in both samples are reasonably consistent with an ideal value of 0.66 in three site jumps. Therefore, experimental values in both samples show that most stems participate in dynamics. It should be noted that $\langle\tau_c\rangle$ in the ordered packing structures for $i\text{PP}_{\Delta T34}$ is 35-fold longer than that in the disordered packing ones for $i\text{PP}_{\Delta T84}$, respectively. The β value of 0.64 corresponds to a distribution

width of ~ 1.0 decade. Figure 9(b) shows temperature dependences of $\langle\tau_c\rangle$ and distribution width for $i\text{PP}_{\Delta T34}$ (●) and for $i\text{PP}_{\Delta T84}$ (O), and both results show Arrhenius behaviors. The best-fitted results to the experimental data show an activation energy of $E_a = 102 \pm 5$ and 72 ± 4 kJ/mol for $i\text{PP}_{\Delta T34}$ and $i\text{PP}_{\Delta T84}$, respectively. Our experimental results show that both $\langle\tau_c\rangle$ and E_a highly depend on supercooling, in other words, static structures, $\langle l \rangle$, and packing order.

4. Discussion

4.1. Chain Packing versus Chain Folding in Stereoregular Polymers. There are continuous interests related to chain folding structures in polymer crystals. However, there is no ultimate conclusion on this issue.¹⁹ Here, we extract chain-folding directions from the stem orientations and packing under a hypothesis of adjacent re-entry structures. In the case of stereoregular polymers, chain folding occurs only between isochiral and anticline stems (R_u and R_d or L_u and L_d) or between antichiral and isocline stems (R_u and L_u or R_d and L_d) due to configurational constraints.³³ The probing order–disorder phenomenon of the stem orientations not only provides the stem packing information but also is only an indirect way for evaluating the chain-folding directions.⁴³

Figures 10(a) and (b) show possible trajectory models of the polymer chains in two limiting structures of a full limit order and disorder, respectively. In the former, polymer chains are folded between L_d and R_d or L_u and R_u , within one bilayer. Thus, growing of polymer chains is ordered within one bilayer along the $a \sin \theta$ axis.^{33,43} On the other hand, orientation disorders statistically exist at individual sites in a full limit disorder. Under such a situation, there is no constraint for the chain-folding directions. Therefore, the order–disorder phenomenon of the stem orientations and packing depending on ΔT leads to largely different chain-folding directions between $P2_1/C$ and $C2/C$ symmetries.

According to nucleation theory,¹ at low ΔT , chain folding well develops at the growth front. With increasing ΔT , other chains are also deposited on the growth front, and two different processes compete with each other as a function of supercooling. Consequently, it is suggested that the chain trajectory changes from two to three dimensions with increasing ΔT . Thus, at high ΔT , polymer chains kinetically favor random entry structures (Figure 10(c)) rather than adjacent re-entry ones with random folding directions as shown in Figure 10(b). Unfortunately, packing analysis cannot differentiate these two structures. However, trajectory of the polymer chain obtained from their packing structures depending on ΔT is roughly consistent with one expected from nucleation theory. Cheng et al. very carefully reported regime transitions of $i\text{PP}$ with different isotacticity. In the case of isotacticity, $\langle mmm \rangle = \sim 97\%$, regime I–II and II–III transitions occur at $\Delta T = \sim 40$ and ~ 60 K, respectively.⁴⁴ The maximum value of f_{order} obtained in this work is 62% even at $\Delta T = 34$ K, and our results indicate that f_{order} is saturated around $\sim 60\%$ at $\Delta T \leq 34$ K in regime I. This finding is quite interesting for understanding the actual crystallization process. In regime I, the well-ordered trajectory of polymer chains along the $a \sin \theta$ axis is dominant. However, it is also true that a large amount of disorders are still present ($\sim 40\%$). Such disorders might be the origin from complex factors such as (i) chain-folding direction at the growth front, (ii) entanglements of the melt chains, and (iii) chemical disorders in stereoregularity, regioregularity, and molecular weights. If chain folding occurs across the bilayer, $P2_1/C$ is disrupted and $C2/C$ is allowed. Thus, errors in folding direction result in lowering f_{order} . Our experimental evidence indicates that chain folding errors

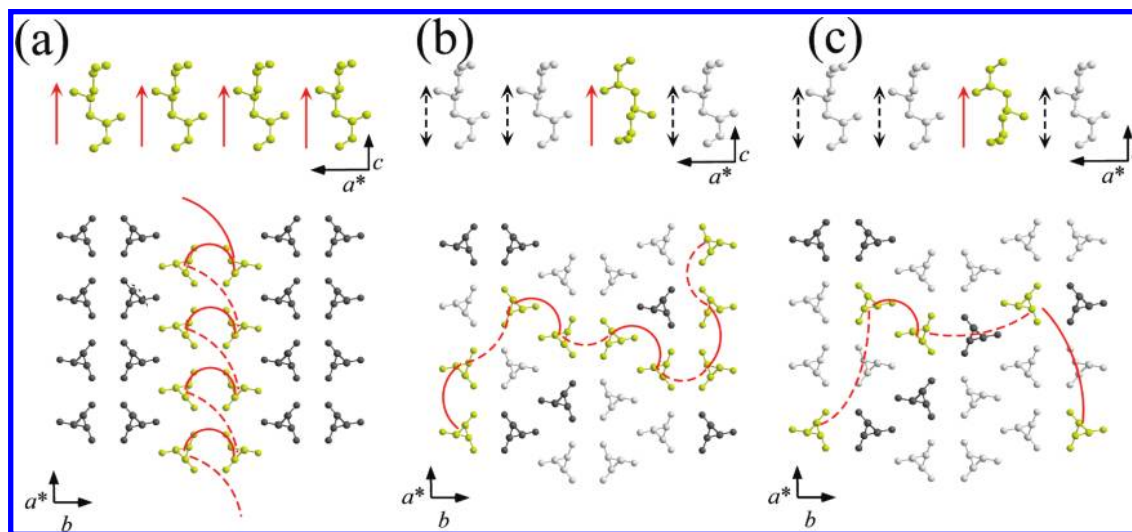


Figure 10. Packing structures of (a) a full limit order and (b) and (c) a full limit disorder versus possible models for trajectory of the polymer chains under a hypothesis of (a) and (b) adjacent re-entry and (c) random entry.

occur even in regime I. Additionally, entanglements in the melt region may decrease f_{order} even at very low ΔT . This effect may be understood in terms of structural analysis of SGC under solution crystallization. There are several works on morphological observations on SGC.^{45,46} SGC commonly shows a lath type morphology, where electron diffraction showed that crystal growth occurs along the $a \sin \theta$ axis, and the unit cell structure shows $P2_1/C$ symmetry. Furthermore, Wittmann and Lotz showed by a decoration method that *i*PP laths are sectorized, and the fold plane in the major sector is along the $a \sin \theta$ axis on ~ 10 nm resolution.⁴⁶ All previous experimental evidence is comparable with the chain-folding direction in a the bilayer model proposed by Corradini et al.⁴³ However, quantitative analysis on f_{order} in SGC is not reported and is a future subject. Molecular weight effect is also related to an entanglement/disentanglement problem. Only Radhakrishnan et al. investigated two samples with one order difference in their M_w .²³ They, however, could not find that there is a significant difference in f_{order} . With regard to chemical disorders, if stems and/or chain folding loops include such disorders, chemical disorders probably influence f_{order} . So far, XRD has been applied for stereoregularity effects. Radhakrishnan et al. indicated that *i*PP with high isotacticity, $\langle mmmm \rangle = 99.4\%$, leads to a full limit order ($f_{\text{order}} = \sim 100\%$).²³ Recently, Nakamura et al. indicated even *i*PP with low isotacticity, $\langle mmmm \rangle$, of 88% also gives a full limit order ($\sim 100\%$).²⁶ XRD analyses by different groups are scattered. The scattering reasons between XRD results were already discussed. Here, our discussions are limited to list up many structural possibilities for the disordered structures even at very high T_c . We are currently investigating these effects on f_{order} by SS-NMR. These results will be published elsewhere.

4.2. Coupling of Molecular Ordering and Dynamics for Lamellar Thickness. The current SS-NMR study clearly demonstrated that time-kinetic parameters and E_a of stem dynamics for the α form of *i*PP highly depend on supercooling. The observed E_a differences between *i*PP_ΔT34 (102 kJ/mol) and *i*PP_ΔT84 (77 kJ/mol) should be interpreted in terms of increases in both $\langle l \rangle$ and ordering of chain packing (*i*PP_ΔT84 with $\langle l \rangle = 9$ nm, $f_{\text{order}} = 0\%$, and *i*PP_ΔT34 with $\langle l \rangle = 19$ nm and $f_{\text{order}} = 62\%$). Enhancement of lamellar thickness leads to an increase of the monomer number of the crystalline stems which participate in dynamics. XRD analysis demonstrated that low supercooling leads to a shrink of the crystal unit-cell parameters along $a \sin \theta$ and b axes by 1–2%.⁴⁷ Actually, we

cannot separate the packing ordering effects on dynamics from the lamellar thickness effect. However, both static structures with different dimensions and length scales can reasonably explain the observed dynamic variations of the stems depending on supercooling.

Mobility plays an important role for thickness enhancement. Thin lamellae consisting of the disordered packing will be thicker by annealing at high temperatures. This point was confirmed by annealing (Figure 7(b)). Actually, $\langle l \rangle$ is significantly enhanced after rearrangement of the polymer chains inside of the crystals after melt and recrystallization. This fact means that not only mobility but also ordering of the trajectory of polymer chains play important roles in lamellar thickness enhancement under crystallization and annealing.

Here, we consider how molecular dynamics and molecular ordering contribute to lamellar thickness enhancement. At very low ΔT , trajectory of the polymer chains is well ordered within one bilayer. Probably, this condition is close to chain trajectory in SGC. Many adjacent stems are properly connected by chain folding. Under such a structural condition, neighboring stems connected by chain folding colored by yellow in Figure 10(a) can cooperatively move along the c axis, thus local helical jumps of stems effectively result in chain diffusions. At high ΔT , chain-folding directions of the polymer chains are randomized, and random entry (Figure 10(c)) or switchboard structures are kinetically favored. Under such conditions, even though local helical jump motions of individual stems show relatively fast dynamics in thin lamellae, cooperativity between the adjacent stems is rare due to fewer connectivities by irregular chain folding (Figures 10(b) and (c)). Thus, local helical jumps of stems do not lead to cooperative chain diffusions between the crystalline and amorphous regions. Very recently, Rastogi et al. detected such a decoupling and coupling between locally helical jumps and chain diffusions in PE in different morphology.^{16,17} Under decoupled conditions, crystal lamellae thickness no longer can develop to a large size. Therefore, coupling of stem dynamics under well-ordered arrangement of the polymer chains inside of the crystal lamellae significantly contributes to lamellar thickness variations under isothermal crystallization and annealing. As shown in Figure 5(a), f_{order} highly depends on ΔT . These local ordering variations play quite important roles for $\langle l \rangle$ values. This is a plausible molecular mechanism in $1/\Delta T$ of lamellar thickness of *i*PP.

In the SGC and NC samples of PE, there are significant enhancements in $\langle l \rangle$ by annealing compared to that in MC. Previously, Uehara et al. connected the absence of entanglements of polymer chains to lamellar thickening behaviors in SGC and NC.¹⁵ Rastogi et al. indicated the importance of interfacial rigidity in SGC.^{16,17} These local structures outside of the crystals depending on morphology are highly linked to the arrangement of the polymer chains inside of the crystals. In SGC and NC, well-ordered arrangement of the polymer chains due to adjacent re-entry is expected. On the other hand, it is expected that MC at high ΔT gives a disordered chain arrangement. Therefore, interfacial structures and entanglements are partial structures of the chain trajectory. It is reasonably concluded that ordering of the chain trajectory including polymer chain arrangement inside of the crystals, entanglement, and interfacial structures play important roles for lamellar thickness enhancement in the polymer crystals. Within these structures, we for the first time focused on the local structure inside of the polymer crystals depending on T_c and T_a .

5. Conclusion

We investigated molecular structures and dynamics of the α form of iPP under isothermal crystallization and annealing by mainly SS-NMR. It was found that stem orientations and packing do not show a complete order under isothermal crystallization and annealing, and a large amount of disorders are included in the crystals. Many structural sources of entanglements, chain-folding directions, chemical disorders, and kinetics influence the order-disorder phenomenon of the stem orientations and their packing during crystallization. Such an ordering is highly related to ordering of the chain trajectory depending on ΔT . At low ΔT , the polymer chain gives a highly ordered trajectory in the ordered packing, which leads to cooperative dynamics of stems, which consequently leads to significant enhancement of lamellar thickness, while trajectory of the polymer chains is largely disordered at high ΔT , structural disorder interrupts cooperative dynamics of the adjacent stems, and crystal lamellae thickness could not develop well at high ΔT , although individual stems show high mobility. The ordering of the chain trajectory plays a very important role for cooperative dynamics and lamellar thickening. Probably, the chain-level changes commonly occur in semicrystalline polymers depending on supercooling or annealing temperature (via melt and recrystallization). However, current available techniques cannot access the structural disorders and orders inside of the crystals on molecular levels, except for stereoregular polymers.

Acknowledgment. This work was financially supported by NEDO Nanostructure Polymer Project. The authors are grateful to Dr. Bernard Lotz for helpful discussions and careful correction of the manuscript.

References and Notes

- Hoffmann, J. D.; Miller, R. L. *Polymer* **1997**, *38*, 3151–3212.
- Cheng, S. Z. D.; Lotz, B. *Polymer* **2005**, *46*, 8662–8681.
- Mezghani, K.; Campbell, R. A.; Phillips, P. J. *Macromolecules* **1994**, *27*, 997–1002.
- Rastogi, S.; Spoelstra, A. B.; Goossens, J. G. P.; Lemstra, P. J. *Macromolecules* **1997**, *30*, 7880–7889.
- Loos, J.; Tian, M.; Rastogi, S.; Lemstra, P. J. *J. Mater. Sci.* **2000**, *35*, 5147–5156.
- Hikosaka, M. *Polymer* **1987**, *27*, 1257–1264.
- Hikosaka, M. *Polymer* **1990**, *31*, 458–468.
- Hikosaka, M.; Amano, K.; Rastogi, S.; Keller, A. *J. Mater. Sci.* **2000**, *35*, 5157–5168.
- Schmidt-Rohr, K.; Spiess, H. W. *Macromolecules* **1991**, *24*, 5288–5293.
- Hu, W. G.; Boeffel, C.; Schmidt-Rohr, K. *Macromolecules* **1999**, *32*, 1611–1619.
- Schaefer, D.; Spiess, H. W.; Suter, U. W.; Fleming, W. W. *Macromolecules* **1990**, *23*, 3431–3439.
- Kentgens, A. P. M.; de Boer, E.; Veeman, W. S. *J. Chem. Phys.* **1987**, *87*, 6859–6866.
- Schmidt-Rohr, K.; Spiess, H. W. *Multidimensional Solid-state NMR and Polymers*; Academic Press: London, 1994.
- Miyoshi, T.; Pascui, O.; Reichert, D. *Macromolecules* **2004**, *37*, 6460–6471.
- Uehara, T.; Yamanobe, T.; Komoto, T. *Macromolecules* **2000**, *33*, 4861–4870.
- Yao, Y. F.; Graf, R.; Spiess, H. W.; Lippits, D. R.; Rastogi, S. *Phys. Rev. E* **2007**, *76*, 060801–1060801–4.
- Yao, T. F.; Graf, R.; Spiess, H. W.; Rastogi, S. *Macromolecules* **2008**, *41*, 2514–2518.
- Sadler, D. M.; Keller, A. *Science* **1979**, *203*, 263–265.
- Kaji, K. *Applications of Neutron Scattering to Soft Condensed Matter, Crystalline and Amorphous Polymers*; Gordon and Breach Science Publishers: New York, 2000; Chapter 5.
- Mencik, Z. *J. Macromol. Sci. Phys.* **1972**, *B6*, 101–115.
- Hikosaka, M.; Seto, T. *Polym. J.* **1973**, *5*, 111–127.
- Napolitano, R.; Pirozzi, B.; Varriale, V. *J. Polym. Sci., Part B: Polym. Phys.* **1990**, *28*, 139–147.
- Radhakrishnan, J.; Ichikawa, K.; Yamada, K.; Toda, A.; Hikosaka, M. *Polymer* **1998**, *39*, 2995–2997.
- Naiki, M.; Kikkawa, T.; Endo, Y.; Nozaki, K.; Yamamoto, T.; Hara, T. *Polymer* **2000**, *42*, 5471–5477.
- Auriemma, F.; de Ballesteros, O. R.; De Rosa, C.; Corradini, P. *Macromolecules* **2000**, *33*, 8764–8774.
- Nakamura, K.; Shimizu, S.; Umemoto, S.; Thierry, A.; Lotz, B.; Okui, N. *Polym. J.* **2008**, *40*, 915–922.
- Miyoshi, T.; Hu, W.; Hagihara, H. *Macromolecules* **2007**, *40*, 6789–6792.
- Bunn, A.; Cudby, M. E. A.; Harris, R. K.; Packer, K. J.; Say, B. J. *Polymer* **1982**, *23*, 694–698.
- Saito, S.; Moteki, Y.; Nakagawa, M.; Horii, F.; Kitamaru, R. *Macromolecules* **1990**, *23*, 3256–3260.
- Caldas, V.; Brown, G. R.; Nohr, R. S.; Macdonald, J. G. *J. Polym. Sci., Part B: Polym. Phys.* **1996**, *34*, 2085–2098.
- Aoki, A.; Asakura, T. *Solid State NMR of Polymers*; Elsevier Science, 1998; pp 415–444, Chapter 11.
- Bennett, A. E.; Rienstra, C. M.; Auger, M.; Lakshmi, K. V.; Griffin, R. G. *J. Chem. Phys.* **1995**, *103*, 6951–6958.
- Petraccone, V.; Pirozzi, B.; Meille, S. V. *Polymer* **1986**, *27*, 1665–1668.
- deAzevedo, E. R.; Hu, W. G.; Bonagamba, T. J.; Schmidt-Rohr, K. *J. Am. Chem. Soc.* **1999**, *121*, 8411–8412.
- VanderHart, D. L.; Alamo, R. G.; Nyden, M. R.; Kim, M. H.; Mandelkern, L. *Macromolecules* **2000**, *33*, 6078–6093.
- Takahashi, T.; Kawashima, H.; Sugisawa, H.; Baba, T. *Solid State NMR* **1999**, *15*, 119–123.
- Takegoshi, K. *Annu. Rep. NMR Spectrosc.*, **1995**, *30*, 97–126.
- Clauss, J.; Schmidt-Rohr, K.; Spiess, H. W. *Acta Polym.* **1993**, *44*, 1–17.
- Maiti, P.; Hikosaka, M.; Yamada, K.; Toda, A.; Gu, F. *Macromolecules* **2000**, *33*, 9069–9075.
- Yamada, K.; Hikosaka, M.; Toda, A.; Yamazaki, S.; Tagashira, K. *Macromolecules* **2003**, *36*, 4790–4801.
- Yamada, K.; Hikosaka, M.; Toda, A.; Yamazaki, S.; Tagashira, K. *Macromolecules* **2003**, *36*, 4802–4812.
- Nakai, T.; Ashida, J.; Terao, T. *Magn. Reson. Chem.* **1989**, *27*, 666–668.
- Corradini, P.; Giunichi, G.; Petraccone, V.; Pirozzi, B.; Vidal, H. M. *Gazz. Chim. Ital.* **1980**, *110*, 413–418.
- Janimak, J. J.; Cheng, S. Z. D.; Giusti, P. A.; Hsieh, E. T. *Macromolecules* **1991**, *24*, 2253–2260.
- Sauer, J. A.; Morrow, D. R.; Richardson, G. C. *J. Appl. Phys.* **1965**, *36*, 3017–3021.
- Wittmann, J. C.; Lotz, B. *J. Polym. Sci., Polym. Phys. Ed.* **1985**, *23*, 205–226.
- Cheng, S. Z. D.; Janimak, J. J.; Zhang, A.; Hsieh, E. T. *Polymer* **1991**, *32*, 648–655.